



High-speed laser cladding of chromium carbide reinforced Ni-based coatings

Jari Tuominen¹ · Jouko Kiviö² · Clara Balusson¹ · Lassi Raami¹ · Jorma Vihinen² · Pasi Peura¹

Received: 6 February 2023 / Accepted: 26 June 2023
© The Author(s) 2023

Abstract

Fusion-bonded and low-diluted overlay welded coatings are frequently very thick (>1mm). High-speed laser cladding is a novel process capable of producing thin fusion-bonded and low-diluted coatings with high coverage rates and low heat input. In this study, for the first time, high-speed laser cladding was used to fabricate relatively thin Ni-based coatings reinforced with chromium carbides onto low-alloy structural and quenched and tempered steels. Obtained coatings were characterized with X-ray diffraction (XRD), optical (OM), and scanning electron microscopy (SEM), as well as electron backscatter diffraction (EBSD). Mechanical and wear properties were tested with Vickers microhardness measurements and three-body dry-sand rubber wheel abrasion tests (RWAT). It was shown that high-speed laser cladding produces 0.2–0.3-mm-thick coatings, which consist of ultrafine-substructured hypereutectic M_7C_3 structures reinforced with coarser primary Cr_3C_2 particles. Coatings with hardness up to 1300 HV_{0.05} exhibited high wear resistance in low-stress three-body abrasion. Coatings developed can be used as alternatives for hard-chrome plated coatings.

Keywords High-speed laser cladding · Hardfacing · Metal matrix composite · Three-body abrasion · Hard-chrome

1 Introduction

Fusion-bonded and low-diluted overlay welded coatings typically range from 1 mm to several millimeters in thickness [1], which results in high material consumption (kg/m^2) and expenses. Extreme high-speed laser cladding (EHLA) and earlier introduced high-speed laser cladding are methods capable of producing thinner overlay welded coatings [2, 3]. Both processes utilize high energy densities using small laser beam spots 1–2 mm in diameter. Instead of plasma-transferred arc (PTA) grade powder (~50–150 μm), the EHLA process uses smaller powder granulometry (~10–60 μm), which enables narrow powder focus. In addition,

laser and powder focus locates just above the melt pool in the EHLA process, increasing the energy absorbed by the powder and decreasing the amount of energy absorbed by the base material.

Coating materials utilized in high-speed laser cladding have varied from soft Ni-based superalloys to harder martensitic stainless steels [2–8]. The ultimate objective has been to develop crack-free alternatives to environmentally hazardous hard-chrome plating [9]. Maximum hardness values reached so far have been limited to ~600 HV, which is clearly lower than those reported for hard-chrome plated coatings 800–1250 HV [10, 11]. This could be the reason why wear comparison between hard-chrome and developed EHLA coatings has not been reported yet. Besides the ability to fabricate thin fusion-bonded coatings, the benefits of high-speed laser cladding include high coverage rates (m^2/h), high solidification rates, low heat input into base material, and high process energy efficiency due to low heat conduction losses. Coverage rate of ~7 m^2/h was recently reached for ~100- μm -thick coating using 8-kW laser power [12]. High solidification rates lead to fine grain structure, which provides hardness increase via grain boundary strengthening. Low heat input diminishes the depth of heat-affected zone (HAZ) and distortion.

Recommended for publication by Commission I - Additive Manufacturing, Surfacing, and Thermal Cutting

✉ Jari Tuominen
jari.tuominen@tuni.fi

¹ Materials Science and Environmental Engineering, Tampere University, Tampere, Finland

² Automation Technology and Mechanical Engineering, Tampere University, Tampere, Finland

Orthorhombic chromium carbide (Cr_3C_2) is a T_m ~1800°C melting point refractory possessing a high degree of chemical stability and is widely used as a reinforcement in overlay welded coatings due to its high hardness [13]. In overlay welding, it typically melts and precipitates as hard hexagonal close-packed (hcp) Cr_7C_3 and face centered cubic (fcc) Cr_{23}C_6 or mixed M_7C_3 and M_{23}C_6 secondary carbides [14–21]. Chromium carbide reinforced overlay welded coatings have been developed, for instance, for cutting knives [22], nuclear reactor components [16], well drilling and oil extraction equipment [19], dies and molds [15], hot rolling mill rolls [20], and boiler tubes [23]. The developed coatings have been found to improve significantly high temperature (HT) sliding wear resistance of cast steels [20], HT oxidation and erosion-corrosion resistance of martensitic stainless steel [15, 19], and sliding wear resistance of austenitic stainless steel [18]. Compared to frequently used tungsten, titanium, and vanadium carbides, which are significantly harder than chromium carbides [13], the benefits of chromium carbides include resistance to high temperature oxidation [15, 24], and it does not belong to the EU's critical list of materials [25].

The objective of this study was to develop thin and hard (>600 HV) overlay welded coatings by high-speed laser cladding similar to the EHLA process. Powder feedstocks used were Ni-based alloy reinforced with different types and volume fractions of chromium carbides. The obtained coatings were tested with a low-stress three-body abrasion tester.

2 Materials and methods

The powder feedstocks used for high-speed laser cladding were (1) Amperit®595.074 and (2) mechanical mixtures of Amperit®380 and Metco 70F-NS (56/44 and 83/17 in wt%). Amperit®595.074 is agglomerated and sintered mixture of NiCrMoNb alloy and Cr_3C_2 in a 50/50 weight ratio with a particle size of 15–45 μm . Powder morphology is spherical and rather porous as displayed in Fig. 1a–b. According to X-ray diffraction (XRD) analysis, Amperit®595.074 consists of γ -Ni, Cr_7C_3 , Cr_3C_2 , and NbC as illustrated in Fig. 2. In Fig. 1b, darker regions are chromium carbides and lighter regions are Ni-based matrices as revealed by the EDS elemental maps. The size of carbides varied from 1 to 8 μm . Amperit®595.074 was also mechanically mixed with Amperit®380 to make the coating more ductile (Amperit®595.074 + Amperit®380 (77/23 wt%)). Metco 70F-NS is sintered and crushed Cr_3C_2 powder rather dense and angular in morphology as shown in Fig. 1c–d. It consists of Cr_3C_2 with the particle size of 5–45 μm . Amperit®380 shown in Fig. 1e is a gas atomized Ni-based alloy with the particle size of 15–45- μm composition corresponding to Inconel 625 [26]. All the mechanical powder mixtures were mixed in the Turbula T2C mixer for 24 h. Theoretical carbon contents

and compositions of used powders are given in Ni/CrC volume fractions in Table 1. The base materials employed for the process parameter optimization were S355 and 42CrMo4 rods with a diameter of 100 mm and length of 500 mm. They were in turned condition. 42CrMo4 was quenched and tempered to a hardness of ~300 HV. Wear test specimens were clad on grit-blasted plates of S355 with the size of 20 × 20 × 50 mm³.

High-speed laser cladding experiments were performed using a continuous wave fiber laser (Coherent C-LASE 3000, Corelase Oy, Finland) with a maximum power of 3 kW. The experimental set-up consisted of a 400- μm fiber, 160-mm collimator unit, f250 optics, a coaxial powder feeding nozzle (Coax14V5 from Fraunhofer IWS), a rotating disc type of powder feeder (Oerlikon Metco Twin 150), and CNC-controlled lathe. Before cladding, turned rods were degreased with ethanol. The varied cladding parameters to produce fusion-bonded coatings with low dilution are summarized in Table 1. Wear test specimens were clamped to a processing table of Fanuc F-200iB parallel kinematic robot keeping the optics and powder feeding nozzle static.

The microstructure of the specimens was studied by applying optical microscopy (OM) and scanning electron microscopy (SEM, Jeol JSM-IT500). The polished coating specimens were etched with a 4% Nital to reveal the HAZ. Energy-dispersive X-ray spectroscopy (EDS) was employed to analyze local chemical compositions and to create elemental maps. Electron back-scattered diffraction (EBSD) was used to detect phases in the microstructure. EBSD specimens were polished using a 0.02- μm colloidal silica suspension. Data acquisition for EBSD was done by using a Zeiss Ultra Plus field emission scanning electron microscope (FESEM) equipped with a Symmetry® EBSD detector (Oxford Instruments). The data was acquired with the step size of 0.7 μm over a 40 μm × 60 μm area by using an acceleration voltage of 15 kV. The collected data was analyzed by using Channel 5 EBSD software. To reveal crystal structures and phases present in the studied materials, an X-ray diffractometer (Panalytical Empyrean Multipurpose Diffractometer) was used. Phase quantifications were made with ImageJ software. Analyzed areas were ~300 × 200 μm^2 for primary carbides and ~30 × 40 μm^2 for secondary carbides. The Vickers microhardness measurements from the coating cross-sections and surfaces were taken with a Matsuzawa MMT-X7 hardness tester using indentation loads of 50 and 1000 g applied for 15 s. Microhardness measurements were also conducted separately on the primary carbides with a load of 50 g.

Three-body abrasion wear tests at room temperature were conducted with a rubber wheel abrasion test device, a modified version of ASTM G65, where crushed dry quartz (SiO_2) sand abrasives (0.1–0.6 mm) flow between the surfaces of the rotating rubber wheel (Durometer A84-88) and the test specimen. The test device and parameters are described in more detail in

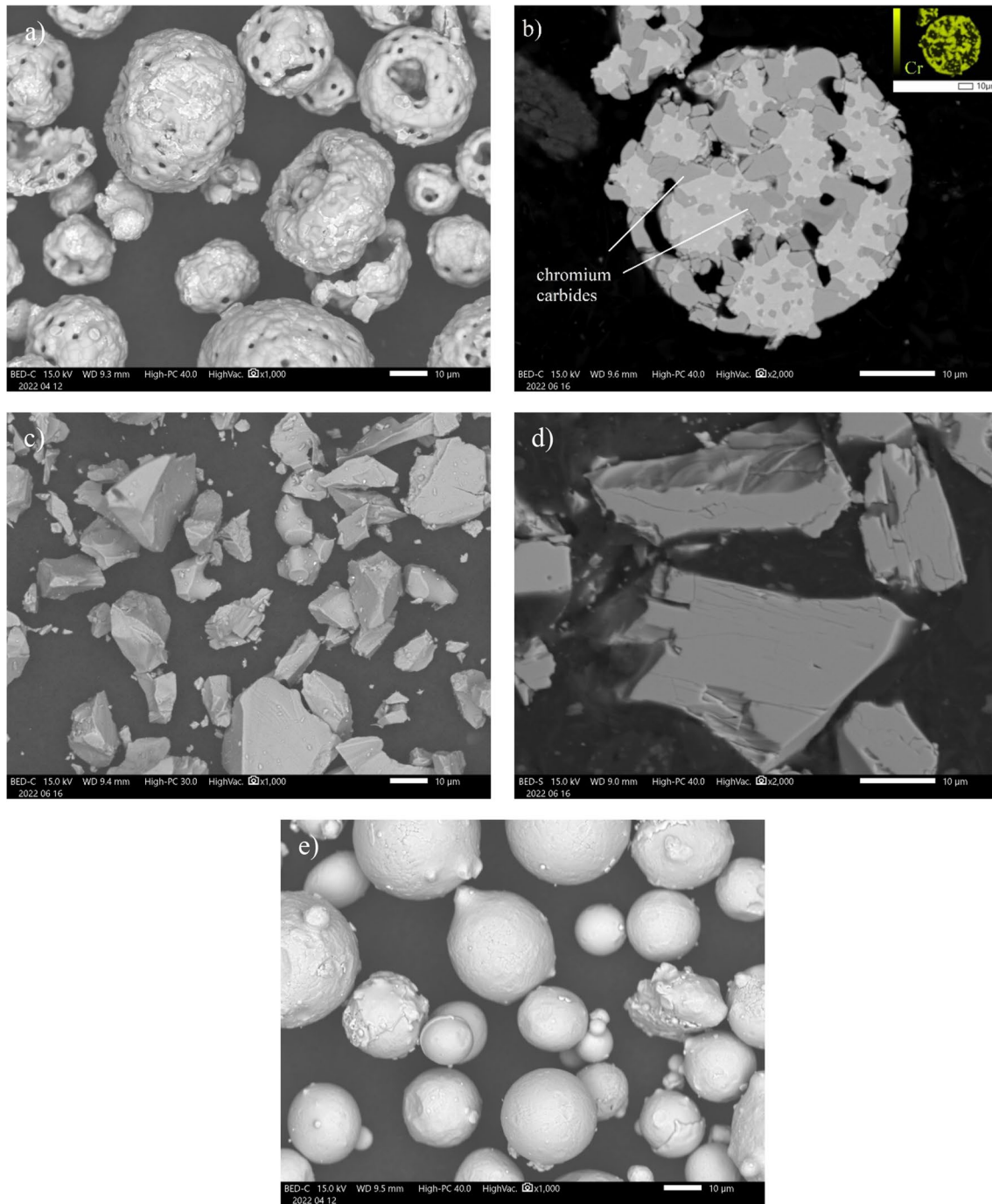


Fig. 1 SEM micrographs of powders. **a, b** Amperit@595.074. **c, d** Metco 70F-NS. **e** Amperit@380

Ref. [27]. Before wear testing, all the laser-clad surfaces were ground with grit #600 and #1200 SiC papers. Commercial hard-chrome plating with the surface hardness of ~ 950 HV_{0.3} was used as a reference material. The worn specimen surfaces were examined by SEM. Wear performance was evaluated as volume loss using theoretical densities for high-speed laser-clad coatings and an average density value of 7.05 g/cm³ found in the literature for the hard-chrome plated coating.

3 Results

3.1 Microstructure

The representative low-magnification OM images of coatings manufactured with process parameters given in Table 1 are illustrated in Fig. 3a–d. Coatings are generally characterized by very low geometrical dilution, narrow HAZ, a

thickness of ~0.2–0.3 mm, and varying amounts of vertical cracks, which stop at the fusion line and do not propagate to the base material. These essential coating characteristics, together with some key process characteristics calculated from the coating dimensions, are shown in Table 2. It can be, for instance, seen that cracking tendency is significantly lower in the coatings fabricated from the coarser sintered

and crushed chromium carbides (#3, #4) than in the coatings produced from agglomerated and sintered powders (#1, #2). Dilutions/penetrations in the beginning of the clads are locally very high when the laser beam hits to fully exposed base material. Later, when the overlapping starts, i.e., after the first bead, the dilution/penetration remains low. This deep penetration region was included in the geometrical

Fig. 2 XRD patterns of Amperit@595.074 and Metco 70F-NS powders

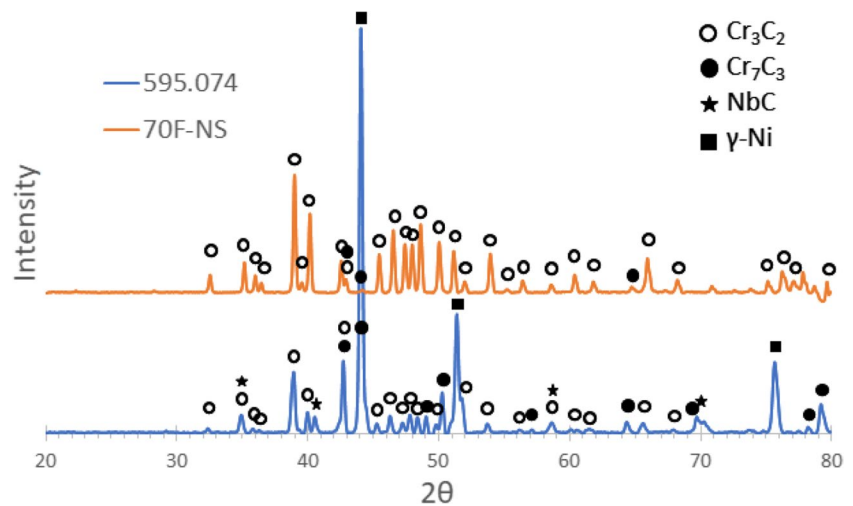


Table 1 High-speed laser cladding process parameters

Designation	Powder	Power (kW)	Theoretical C content (wt%)	Traverse speed (m/min)	Powder feed rate (g/min)
#1	595.074 (Ni/CrC 44/56 vol%)	2.0	6.7	25	7
#2	380 + 595.074 (Ni/CrC 56/44 vol%)	2.0	5.2	25	8
#3	380 + 70F-NS (Ni/CrC 50/50 vol%)	1.9	5.9	25	8
#4	380 + 70F-NS (Ni/CrC 80/20 vol%)	1.9	2.3	25	11

Fig. 3 Low magnification OM images of coatings. **a** Amperit@595.074. **b** Amperit@595.074 + Amperit@380 (77/23 wt%). **c** Amperit@380 + Metco 70F-NS (56/44 wt%). **d** Amperit@380 + Metco 70F-NS (83/17 wt%)

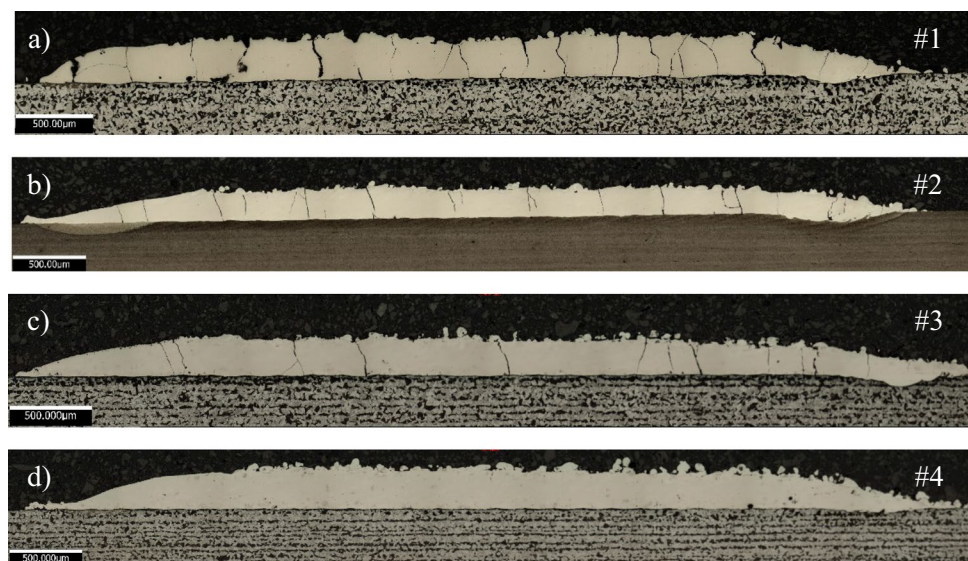
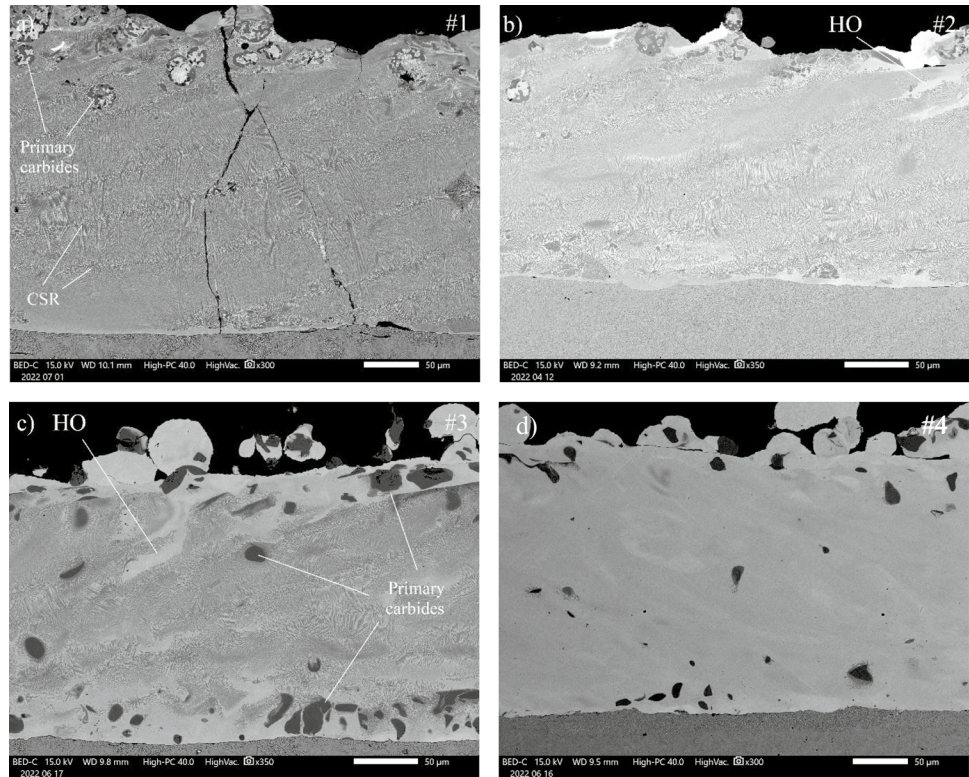


Table 2 Summary of coating and process characteristics. Standard deviation for crack density is given in parentheses

Coating	Dilution	Effective coating thickness	Depth of HAZ	Crack density	Powder efficiency	Coverage rate	Powder consumption
#1	1.9%	0.23mm	~30 μ m	5.2 mm ⁻¹ (1.3)	74%	0.2m ² /h	2.2kg/m ²
#2	3.9%	0.19mm	~50 μ m	3.2 mm ⁻¹ (0.8)	56%	0.2m ² /h	2.4kg/m ²
#3	2.4%	0.20mm	~50 μ m	2.4 mm ⁻¹ (0.6)	61%	0.2m ² /h	2.2kg/m ²
#4	1.9%	0.24mm	~30 μ m	0.2 mm ⁻¹ (0.1)	60%	0.2m ² /h	2.9kg/m ²

Fig. 4 High magnification SEM images of coatings. **a** Amperit@595.074. **b** Amperit@595.074 + Amperit@380 (77/23 wt%). **c** Amperit@380 + Metco 70F-NS (56/44 wt%). **d** Amperit@380 + Metco 70F-NS (83/17 wt%). The lightest regions pointed by arrows HO are hypoeutectic regions in otherwise hypereutectic structures. CSR stands for coarser structure region



dilution calculations. The effective coating thickness given in Table 2 is the minimum coating thickness, i.e., the thickness that remains after the necessary machining operation to get the smooth surface without as-clad remnants [28].

High magnification SEM images shown in Fig. 4 reveal that most of the chromium carbides melted due to a relatively low melting point (~1800°C) and high solubility to nickel matrix and precipitated as needle-like secondary carbides. The amounts of primary and secondary carbides in the coatings are tabulated in Table 3. The volume fractions of primary carbides are significantly higher in coatings fabricated from coarser sintered and crushed chromium carbides (#3, #4) than in coatings made of finer carbides (#1, #2). This was an expected result since coarser carbides offer a smaller surface area to volume ratio than finer carbides making them less vulnerable to melting. This observation of survived primary carbides differs a bit from the results reported in Refs. [23, 29], where the complete melting of

Table 3 Volume fraction of primary and secondary carbides

Coating	Primary	Secondary
#1	1.3 vol% 0.2 STDEV	61.6 vol% 0.5 STDEV
#2	0.8 vol% 0.1 STDEV	46.9 vol% 0.4 STDEV
#3	5.4 vol% 1.4 STDEV	43.4 vol% 0.4 STDEV
#4	2.6 vol% 0.7 STDEV	16.0 vol% 5.0 STDEV

fine primary carbides made of agglomerated and sintered powder took place in conventional laser cladding. Complete melting can be attributed to a significantly longer interaction time between the laser beam and the material in conventional than in high-speed laser cladding.

Interaction times calculated by beam diameter divided by traverse speed in Refs. [23, 29] were 0.125–0.750 s compared to 0.0029 s used in this work. According to XRD scans and EBSD analyses, these secondary needle-like carbides

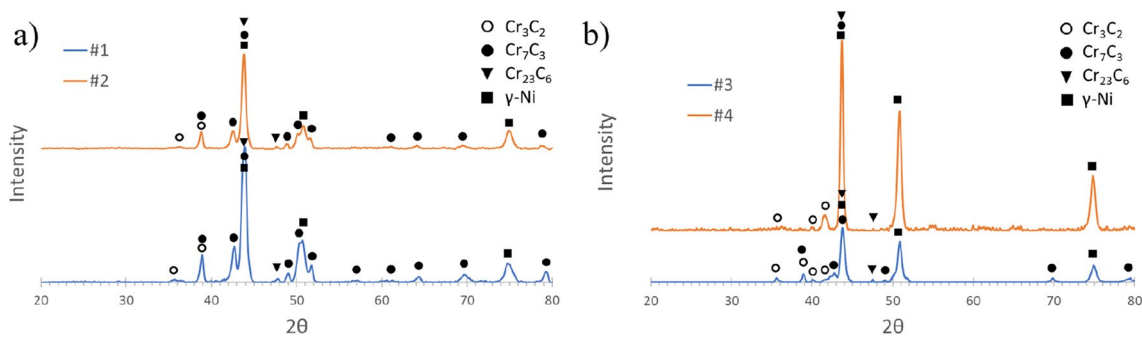


Fig. 5 XRD patterns of coatings. **a** Amperit@595.074 (#1) and Amperit@595.074 + Amperit@380 (77/23 wt%) (#2). **b** Amperit@380 + Metco 70F-NS (56/44 wt%) (#3) and Amperit@380 + Metco 70F-NS (83/17 wt%) (#4)

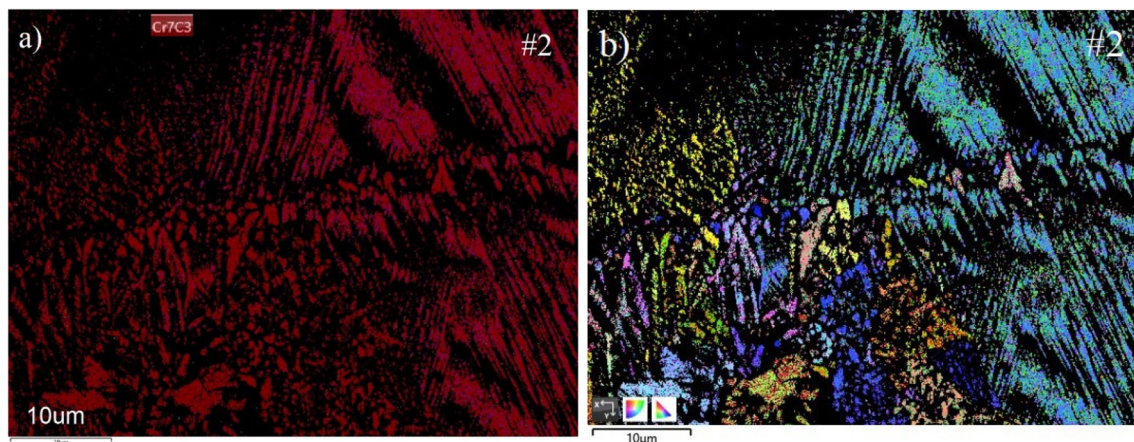


Fig. 6 High magnification EBSD images of Amperit@595.074 + Amperit@380 (77/23 wt%) coatings. **a** Phase color. **b** IPF. Red regions in **a** are Cr_7C_3 or M_7C_3 carbides

are mainly Cr_7C_3 and to a lesser extent Cr_{23}C_6 as displayed in Figs. 5 and 6a. According to Gibbs free energy of formation values in the temperature range 700–900°C, Cr_7C_3 (–140 to –130 kJ/mol) and Cr_{23}C_6 (–340 to –320 kJ/mol) are thermodynamically more stable than Cr_3C_2 (–80 to –70 kJ/mol) [30]. The more abundant existence of M_7C_3 than M_{23}C_6 , which is thermodynamically less stable than M_{23}C_6 , can be justified by stoichiometry and kinetics. According to the theoretical chemical compositions of the matrix given in Table 4, carbide former (Cr, Mo, Nb) ratio to carbon is very close to Cr_7C_3 (= 91.0 wt% Cr, 9.0 wt% C, Cr/C ratio: 91.0/9.0 = 10.1) in coatings #1, #2, and #3. After the solidification of M_7C_3 , there was not enough time for kinetics-governed diffusion-based $\text{M}_7\text{C}_3 \rightarrow \text{M}_{23}\text{C}_6$ transformation due to rapid cooling, which explains the low content of M_{23}C_6 .

According to an inverse pole figure (IPF) image, there is a strong preferred orientation of grains in the secondary carbides on the right-hand side of the image in Fig. 6b, whereas carbides are more randomly oriented on the left. As evidenced by the EDS analyses, all the structures are

Table 4 Theoretical chemical compositions (wt%) of matrix and carbide formers (Cr, Nb, Mo) and carbide former ratio to carbon

Coating	Matrix	Carbide formers	Ratio
#1	33.8Ni-53.0Cr-4.6Mo-2.0Nb-6.6C	59.6	9.0
#2	41.1Ni-45.8Cr-5.6Mo-2.5Nb-5.0C	53.9	10.8
#3	39.3Ni-47.6Cr-5.3Mo-2.3Nb-5.5C	55.2	10.0
#4	56.6Ni-30.3Cr-7.7Mo-3.4Nb-2.0C	41.1	20.5

hypereutectic except Amperit@380 + 70F-NS (83/17 wt%) (#4), which is hypoeutectic as displayed in Fig. 7a–b. Secondary carbides locate in this hypoeutectic alloy in the interdendritic/columnar regions as shown in Fig. 7b. The structure is very fine exhibiting secondary dendrite arm spacings (λ_2) as low as $\sim 0.3 \mu\text{m}$, which is orders of magnitude lower than in laser — (3 μm) and cold metal transfer — clad (5 μm) Inconel 625 coatings [31], indicating very high solidification rate [32]. According to a relationship $\lambda_2 = A(dT/dt)^{-n}$, where (dT/dt) is cooling rate, A and n are

material-specific constants, and cooling rate of $\sim 21 \times 10^6$ °C/s was obtained for coating #4 using material constants of 58.02 (A) and 0.312 (n) based on the works of Tinoco and Fredriksson [33]. Coatings #2 and #3 show distinctive hypoeutectic regions (HO) with low secondary carbide content as illustrated well in Fig. 4b and c. According to image analysis, HO regions occupy ~ 14 vol% in coating #3 and ~ 3 vol% in coating #2. Such seemingly low carbide content regions were not detected from Amperit®595.074 (#1) coating, which was more homogeneous in structure in that sense. Some coarser structure regions (CSR) can be, however, detected in Amperit®595.074 (#1) in Fig. 4a. They follow the fusion lines of each individual beads, which are overlapped on each other, and originate from the remelting of the thin layer of the previous bead. Thin featureless layer ~ 3 – 4 μm in thickness just above the fusion line originates from the planar growth where the G/V_s ratio is high. G is thermal gradient (°C/m) and V_s (m/s) is solidification speed at the solid-liquid interface. Occasional single aluminum oxide inclusions less than 1 μm in size were also detected from the coatings as displayed in Fig. 6a.

Chemical composition profiles throughout the coatings were obtained with EDS area analyses. The analyzed areas were ~ 20 μm in diameter. They were taken at 40- μm intervals, as shown in Fig. 8. Besides C, Cr, Fe, Ni, Nb, and Mo, EDS also detected a small amount (< 1.0 wt%) of Al and Si. Carbon contents in the graphs are somewhat exaggerated because EDS cannot quantify lightweight carbon properly [34]. According to theoretical calculations, total carbon concentrations are supposed to be 6.7 wt% for #1, 5.2 wt% for #2, 5.9 wt% for #3, and 2.3 wt% for #4. In theoretical calculations, it was assumed that NiCrMoNb does not include any carbon and Cr_3C_2 consists of 86.7 wt% chromium and 13.3 wt% carbon. Average carbon concentrations measured by EDS from the matrix were 8.3 wt% for #1, 7.1 wt% for #2, 7.1 wt% for #3, and 3.2 wt% for #4. Interestingly, matrices of coatings #2 and #3 contain the same amount of carbon. This similarity is due to the severe melting of fine agglomerated and sintered carbides into the matrix. It is also observed

that Fe concentrations in all the coatings are below 1.0 wt%, which indicates very low chemical dilution. Inter-mixed Fe is also homogeneously distributed across the coating cross-section, which benefits corrosion performance.

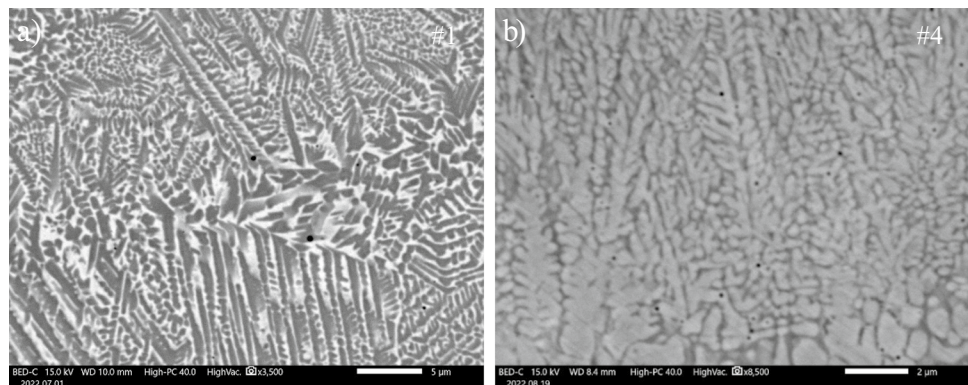
3.2 Microhardness

Hardness profiles measured from the coating cross-sections and hardness values measured from the coating surfaces are illustrated in Fig. 9a–b. Average coating hardness values vary from ~ 500 to ~ 1250 $\text{HV}_{0.05}$ Amperit®595.074 (#1) being the hardest and the Amperit®380+Metco 70F-NS (83/17 wt%) (#4) the softest. According to total carbon contents, Amperit®380+Metco 70F-NS (56/44 wt%) (#3) was expected to be harder than Amperit®595.074+Amperit®380 (77/23 wt%) (#2). Instead, it came out that a higher volume fraction of secondary carbides made the latter (#2) harder due to more severe melting of primary carbides. Hardness values were also measured from the coarser primary carbides made of sintered and crushed powder (70F-NS). They were 1250–1350 $\text{HV}_{0.05}$ being significantly higher than their matrices. Despite apparent brittleness of coatings, none of the coatings exhibited crack initiation from the corners of Vickers pyramid indentation at a load of 1 kg indicating reasonable fracture toughness. Cracks were not detected from the HAZ of 42CrMo4 steel either, even if it hardened strongly. The maximum hardness at HAZ was ~ 600 $\text{HV}_{0.05}$, which is, however, way too high for many applications (power transmission) due to a loss of toughness [35]. The hardness increase of coating #4 near the fusion line in Fig. 9a originates from the indenter partly hit to the unmelted primary Cr_3C_2 .

3.3 Abrasion wear

The rubber wheel abrasion test (RWAT) results are presented in the form of volume losses as a function of time and column chart in Fig. 10a–b. The results are the average of three test runs per studied material. As

Fig. 7 High magnification BSE images of coatings. **a** Hypereutectic Amperit®595.074. **b** hypoeutectic Amperit®380 + Metco 70F-NS (83/17 wt%). Dark phases are chromium carbides and light phases nickel. Tiny black dots are aluminum oxide inclusions



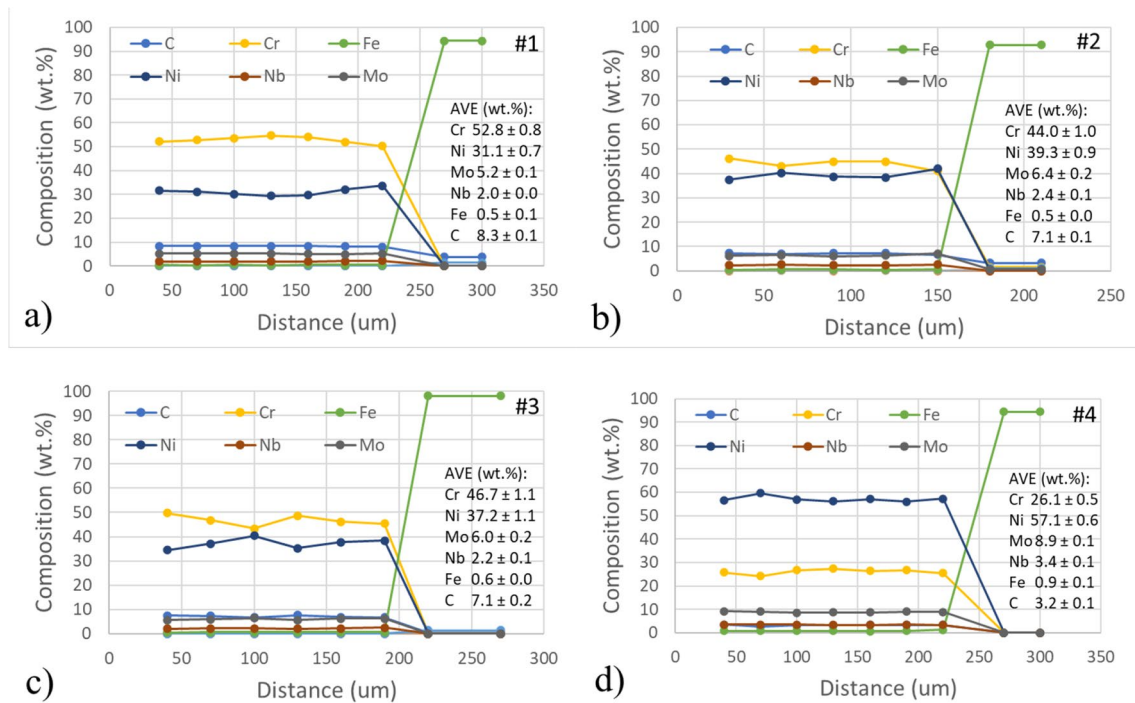


Fig. 8 Chemical composition profiles of coatings obtained by EDS. **a** Amperit®595.074. **b** Amperit®595.074 + Amperit®380 (77/23 wt%). **c** Amperit®380 + Metco 70F-NS (56/44 wt%). **d** Amperit®380 + Metco 70F-NS (83/17 wt%). Error bars (± 0.2 wt%) fall under the markers

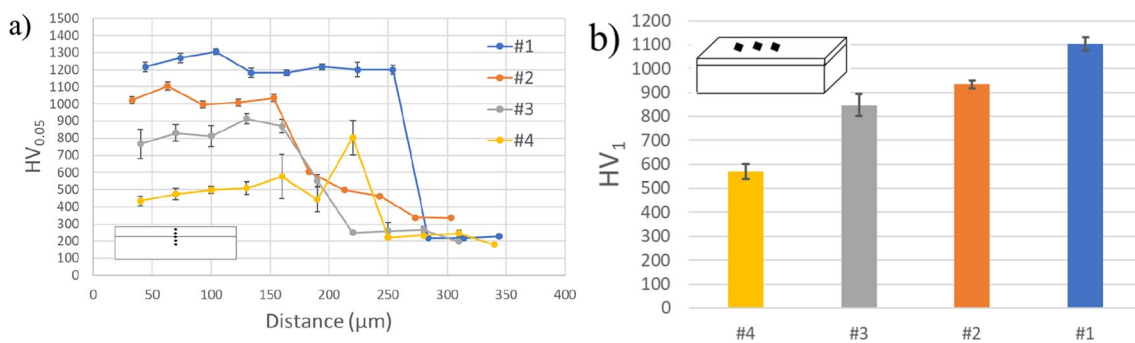


Fig. 9 Hardness values of chromium carbide reinforced Ni-based coatings produced by high-speed laser cladding. **a** Hardness profiles measured from cross-section. **b** Hardness values measured from surface

indicated by the results, the volume removed per unit of sliding time/distance was rather constant throughout the test for each material. It was also found that the differences between different coatings were rather obvious, which suggests that the coatings could be ranked in terms of wear performance. The hardest high-speed laser clad coating, Amperit®595.074 (#1), showed the best while the softest Amperit®380+70F-NS (80/20 vol%) (#4) the worst wear performance. Importantly, the hardest high-speed laser clad coating, Amperit®595.074 (#1), even slightly outperformed or behaved equally with the hard-chrome plated coating in wear resistance.

High magnification SEM images of wear scars are displayed in Fig. 11a–d. The observation of the worn surfaces revealed that the softest coating (~ 550 HV), Amperit®380+70F-NS (80/20 vol%) (#4), showed large wear grooves parallel to the sliding direction caused by micro-ploughing whereas other coatings exhibited only shallow and narrow scratches caused by micro-cutting. The width of the grooves caused by the penetration of hard angular quartz sand particles (~ 750 – 1200 HV) in the softest coating was ~ 600 μ m. According to criteria $H_{\text{abrasive}}/H_{\text{material}} > 1.2$ given in Ref. [11], abrasion conditions were hard for this coating. Wear scar of the softest coating showed also strong signs of plastic deformation

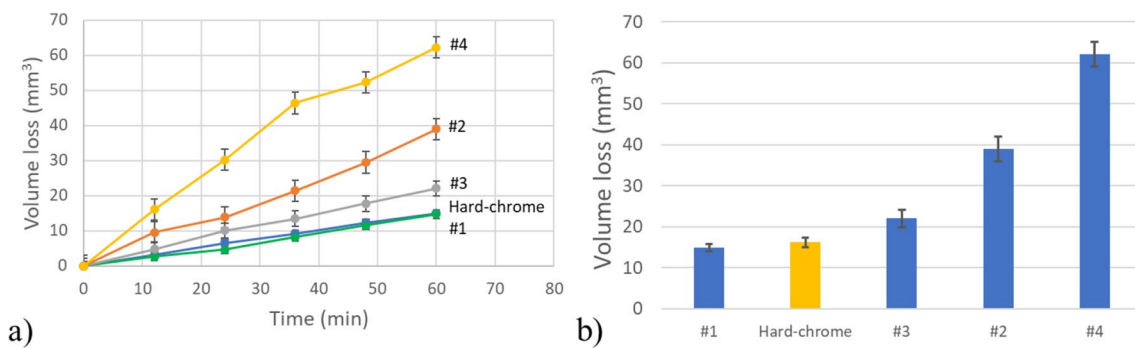
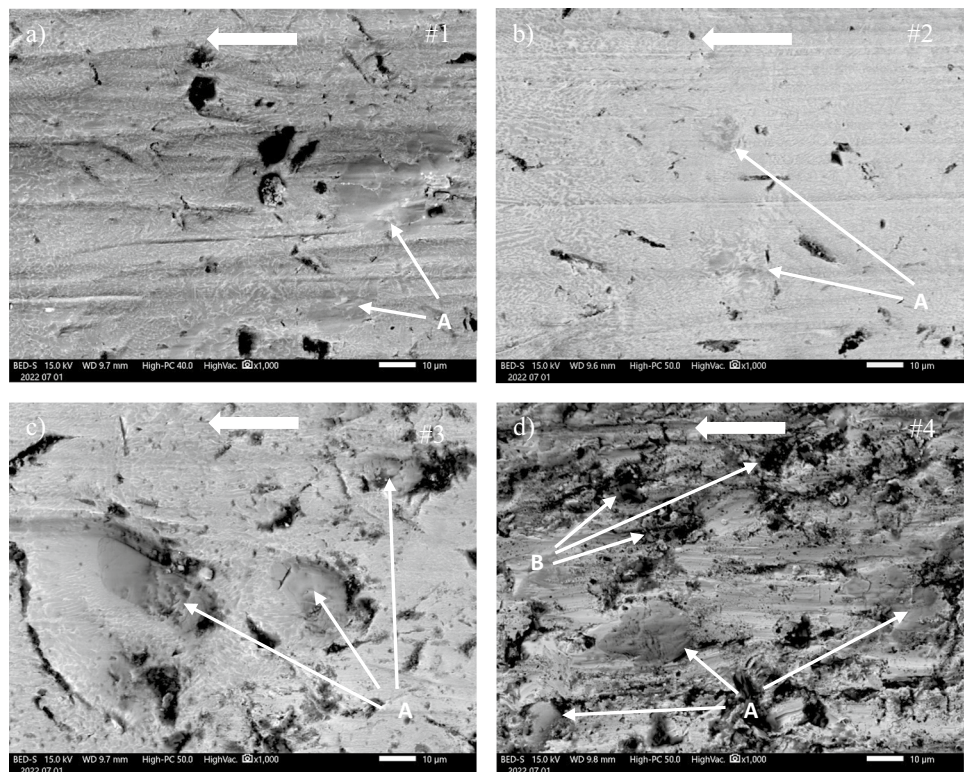


Fig. 10 Volumetric wear losses of chromium carbide reinforced Ni-based coatings. **a** As a function of time. **b** In total

Fig. 11 High magnification SEM images of wear scars. **a** Amperit®595.074. **b** Amperit®595.074 + Amperit®380 (77/23 wt%). **c** Amperit®380 + Metco 70F-NS (56/44 wt%). **d** Amperit®380 + Metco 70F-NS (83/17 wt%) coatings. Primary chromium carbides providing high local wear resistance are pointed by arrow A. The darkest regions pointed by arrows B are remnants of quartz sand (Si, O). Wear direction is indicated by white arrow



and a large amount of adhered quartz on the surface as shown in Fig. 11d. It is also seen that occasional primary Cr_3C_2 particles, even if slightly cracked, exhibited high local wear resistance since they clearly protruded from the matrix. The mean free path between carbides ($\sim 290 \mu\text{m}$) is, however, too long to prevent the penetration of quartz sand abrasives ($0.1\text{--}0.6 \text{ mm}$) due to the low volume fraction of primary carbides. Such non-uniform or preferential matrix wear was much less distinctive in the coatings (#1, #2) reinforced with agglomerated and sintered chromium carbides due to a smaller hardness difference between the primary carbide and the matrix.

The addition of a higher volume fraction (50 vs. 20 vol%) of dense sintered and crushed Cr_3C_2 improved

the wear resistance by a factor of three owing to higher hardness (~ 850 vs. 550 HV) and the shorter mean free path between primary carbides, which was $\sim 230 \mu\text{m}$ in coating #3. Since most of the abrasives were larger than the mean free path, the primary carbides effectively prevented the penetration of abrasives into the softer matrix in coating #3. The protective effect of primary carbides is clearly seen in Fig. 11c, where the matrix wear is much less behind than in the front of the carbide in relation to the wear/sliding direction.

The significant role of the primary carbides in the prevention of abrasive wear emerges strongly when comparing Amperit®380+70F-NS (50/50 vol%) (#3) and Amperit®380+595.074 (#2) coatings. Despite higher

hardness (~930 vs. 850 HV), Amperit®380+595.074 (#2) suffered from significantly higher wear loss due to a lower volume fraction of primary carbides (0.8 vs. 3.6 vol%) and the higher mean free path between carbides (~530 vs. ~230 μm). This finding suggests that the volume fraction of primary carbides should be increased in the coating, for instance, by using 20–45- μm carbide granulometry instead of the 5–45 μm used in this study. The excellence of Amperit®595.074 (#1) is based simply on hardness, which is very close to that of abrasive. High-volume fraction of M_7C_3 chromium carbide is known to be effective particularly in low-stress abrasion conditions [36]. High hardness of M_7C_3 evidently originates from the hcp structure and its low c/a ratio of 0.32 [29], where c and a are lattice parameters. Hardness as high as ~23 GPa (~2300 HV) was reported for Cr_7C_3 in Ref. [29].

4 Discussion

The results showed that high-speed laser cladding can produce relatively thin (0.2–0.3 mm) overlays of Ni-based coatings reinforced with chromium carbides, which are equal to hard-chrome plating in wear resistance. Compared to hard-chrome plated coatings, high-speed laser-clad coatings possess a fusion bond, which is a great benefit and enables the use of coatings also in highly stressed applications where strong adhesion/bonding is required. When considering corrosion protection, the relatively high crack density (5.2 mm^{-1}) in the hardest and the most wear-resistant high-speed laser-clad coatings, as well as in any other available to-date coatings, is obviously a drawback. Interconnected cracks allow corrosive liquids, fumes, and gases to penetrate to the less noble base material and corrode it quickly. On the other hand, thick and hard hard-chrome plated coatings exhibit the same problem [37]. According to Ref. [38], hard-chromes thicker than 10 μm form interconnected macrocracks reaching the base material. Besides macrocracks, hard-chrome plated coatings contain microcracks, which do not initially reach the base material. As was shown in Ref. [38], there is a correlation between microcrack density and microhardness. The harder the hard-chrome plated coating is, the higher the microcrack density appears. Microcrack densities as high as 30–40 mm^{-1} were reported for hard-chrome plated coating ~950 HV in hardness in Ref. [38]. Interconnected cracks lead to rapid deterioration under corrosive environments as was shown in Refs. [39, 40]. Beneficial effects of cracks include relaxation of residual stresses and working as oil pockets in lubricating applications.

In high-speed laser-clad coatings, the cracks encountered in this study are the type of brittle cracks. They evolve

during fast cooling when the hot coating material tries to undergo shrinkage but is prevented by the constraints imposed by the relatively cool and rigid base material and the previous bead. If the resulting shrinkage or thermal stresses exceed the ultimate tensile strength of the coating material and all the deformability/ductility is used up, brittle cracks perpendicular to the coating/base material interface develop relieving tensile residual stresses. The magnitude of these shrinkage or thermal stresses can be roughly estimated in a fully restrained situation with equation [41]:

$$\sigma_{\text{th}} = E \cdot \alpha_{\text{CTE}} \cdot \Delta T_1 \quad (1)$$

where σ_{th} is shrinkage stress (MPa), E is Young's modulus (GPa), α_{CTE} is coefficient of thermal expansion (CTE) (K^{-1}), and ΔT_1 is the difference between melting temperature and base material during processing (K). Roughly estimated, the amount of shrinkage stress in the fully restrained situation could be in the order of ~3500 MPa for coating 50NiCrMoNb-50 Cr_7C_3 in vol% using the values of $E_{\text{Cr}_7\text{C}_3} = 295$ GPa [42], $E_{\text{NiCrMoNb}} = 208$ GPa, $\alpha_{\text{CTE}}(\text{Cr}_7\text{C}_3) = 6.2 \times 10^{-6} \text{ K}^{-1}$ (20–100°C) [42], $\alpha_{\text{CTE}}(\text{NiCrMoNb}) = 12.8 \times 10^{-6} \text{ K}^{-1}$ (20–100°C), and $\Delta T_1 = 1500^\circ\text{C}$. Additional stresses form during further cooling due to the CTE difference between the coating and base material. The magnitude of these stresses can be estimated with an equation (even if it assumes that the coating and base material are both at the same temperature) [43]:

$$\sigma = \frac{(\text{CTE}_c - \text{CTE}_s) \times (T_2 - T_1) \times E_c}{1 - \nu_c} \quad (2)$$

where σ is stress (MPa), CTE_c coefficient of thermal expansion for coating (K^{-1}), CTE_s coefficient of thermal expansion for base material (K^{-1}), T_2 heat treatment or process temperature ($^\circ\text{C}$), T_1 room temperature ($^\circ\text{C}$), E_c Young's modulus of coating (GPa), and ν_c Poisson's number of coating. The equation suggests that forming stresses are tensile if CTE_c is higher than CTE_s and compressive if CTE_c is lower than CTE_s . Assuming that CTE for steels is $12.0 \times 10^{-6} \text{ K}^{-1}$ (20–300°C) and for 50NiCrMoNb-50 Cr_7C_3 in vol% $9.5 \times 10^{-6} \text{ K}^{-1}$ (20–100°C), forming stress caused by CTE difference would be compressive counteracting against the tensile stresses caused by the shrinkage stress. Both equations (1 and 2) also suggest that preheating or elevated cladding temperature has beneficial effect on developing stresses. In high-speed laser cladding, where the base material temperature remains low, residual stresses are presumably higher than in conventional laser cladding, which negatively affect brittle cracking in hardfacing alloys and hot cracking in softer alloys.

Therefore, future research directions need to focus on decreasing the crack density. Preheating and elevated

cladding temperatures should be studied by using, for instance, a closed-looped induction heater [44]. Chromium carbide size distribution should preferably be narrowed from 5 to 45 μm , for instance, to 20–45 μm to prevent excessive melting of carbides and embrittlement of the matrix. Other techniques to improve corrosion resistance are likely to include the use of a thin undercoat fabricated from ductile corrosion-resistant alloy by high-speed laser cladding and the use of sealers to fill in the cracks in a hardfaced layer. Obvious brittleness of coatings sets also needs to study the properties of coatings also in different wear modes such as erosion, high-stress, and impact-abrasion, sliding wear, and determination of coefficient of friction.

5 Conclusions

In the present study, low-diluted and fusion-bonded Ni-based coatings reinforced with different types and volume fractions of chromium carbides were fabricated by the high-speed laser cladding process potentially to replace the hard-chrome plated coatings. After microstructural characterization, microhardness measurements, and wear tests, the following conclusions can be drawn:

1. Fabricated coatings are ~200–300 μm in thickness microhardness varying from 500 to 1300 $\text{HV}_{0.05}$. Most of the added chromium carbides (Cr_3C_2) are melted in the process and precipitated as hard and wear-resistant M_7C_3 carbides forming hypoeutectic and hypereutectic structures.
2. Larger sintered and crushed chromium carbides are more likely to remain unmelted than finer agglomerated and sintered chromium carbides, which makes the coating more metal matrix composite (MMC) like and decreases the susceptibility for embrittlement and cracking.
3. The hardest high-speed laser clad coating exhibited the wear resistance equivalent to hard-chrome plated coating in a low-stress three-body abrasion wear test.

Funding Open access funding provided by Tampere University including Tampere University Hospital, Tampere University of Applied Sciences (TUNI). This research was funded by the European Regional Development Fund, grant number A78522. The project “Fast coating method – Benefits for the industry” is funded by the React-EU Instrument as part of the European Union’s response to the COVID-19 pandemic.

Declarations

Conflict of interest The authors declare no competing interests.

Open Access This article is licensed under a Creative Commons Attribution 4.0 International License, which permits use, sharing, adaptation, distribution and reproduction in any medium or format, as long as you give appropriate credit to the original author(s) and the source, provide a link to the Creative Commons licence, and indicate if changes were made. The images or other third party material in this article are included in the article's Creative Commons licence, unless indicated otherwise in a credit line to the material. If material is not included in the article's Creative Commons licence and your intended use is not permitted by statutory regulation or exceeds the permitted use, you will need to obtain permission directly from the copyright holder. To view a copy of this licence, visit <http://creativecommons.org/licenses/by/4.0/>.

References

1. Silva CC (2013) Weld overlay. In: Wang QJ, Smith RZ (eds) Encyclopedia of tribology. Springer US, Boston, pp 4094–4101
2. Schopphoven T, Gasser A, Wissenbach K, Poprawe R (2016) Investigations on ultra-high-speed laser material deposition as alternative for hard chrome plating and thermal spraying. *J Laser Appl* 28:022501-1–022501-9. <https://doi.org/10.2351/1.4943910>
3. Seefeld T, Theiler C, Sepold G (2001) Laser beam cladding at high processing speed. Proceedings of the ICALEO conference, Jacksonville, USA
4. Yang J, Bai B, Ke H, Cui Z, Liu Z, Zhou Z, Xu H, Xiao J, Liu Q, Li H (2021) Effect of metallurgical behavior on microstructure and properties of FeCrMoMn coatings prepared by high-speed laser cladding. *Opt Laser Technol* 144:107431. <https://doi.org/10.1016/j.optlastec.2021.107431>
5. Wang K, Du D, Liu G, Pu Z, Chang B, Ju J (2020) High-temperature oxidation behaviour of high chromium superalloys additively manufactured by conventional or extreme high-speed laser metal deposition. *Corros Sci* 176:108922. <https://doi.org/10.1016/j.corsci.2020.108922>
6. Lampa C, Smirnov I (2019) High speed laser cladding of an iron based alloy developed for hard chrome replacement. *J Laser Appl* 31:022511-1–022511-4. <https://doi.org/10.2351/1.5096142>
7. Li L, Shen F, Zhou Y, Tao W (2019) Comparative study of stainless steel AISI 431 coatings prepared by extreme-high-speed and conventional laser cladding. *J Laser Appl* 31:022511-1–022511-9. <https://doi.org/10.2351/1.5094378>
8. Zhang X, Sun Y, Yu G, Chen C, Ren X, Chen L (2023) Microstructural evolution and high-temperature oxidation of TiC/IN625 coatings fabricated by multi-layer extreme high-speed laser cladding. *Opt Laser Technol* 158:108838. <https://doi.org/10.1016/j.optlastec.2022.108838>
9. Union E (2013) COMMISSION REGULATION (EU) No 348/2013 of 17 April 2013 amending Annex XIV to Regulation (EC) No 1907/2006 of the European Parliament and of the Council on the Registration Evaluation, Authorisation and Restriction of Chemicals (REACH). *Off J Eur Union* 56:1–5
10. Papatheodorou T (2005) Influence of hard chrome plated rod surface treatments on sealing behavior of hydraulic rod seals. *Sealing Technol*:5–10. [https://doi.org/10.1016/S1350-4789\(05\)00600-8](https://doi.org/10.1016/S1350-4789(05)00600-8)
11. Hutchings IM (1996) Tribology: friction and wear of engineering materials, fourth edn. Arnold, London
12. Vogt S, Göbel M, Fu E (2022) Perspectives for conventional coating processes using high-speed laser cladding. *J Manuf Sci E – T ASME* 144:044501-1–044501-7
13. Pierson HO (1996) Handbook of refractory carbides and nitrides: properties, characteristics, processing, and applications, first edn. Noyes Publications, USA

14. Tassin C, Laroudie F, Pons M, Lelait L (1995) Carbide-reinforced coatings on AISI 316L stainless steel by laser surface alloying. *Surf Coat Technol* 76-77:450–455. [https://doi.org/10.1016/0257-8972\(95\)02613-4](https://doi.org/10.1016/0257-8972(95)02613-4)
15. Kim TH, Kim BC (1992) Chromium carbide laser-beam surface-alloying treatment on stainless steel. *J Mater Sci* 27:2967–2973. <https://doi.org/10.1007/BF01154107>
16. Kumar S, Goswami GL (2006) Wear behaviour of various Ni-based laser clad materials. *Lasers Eng* 16:305–315
17. Kathuria YP (1998) Laser cladding / selective sintering of hard materials. Proceedings of the ECLAT, Hannover, Germany
18. Betts JC (2009) The directed laser deposition of AISI316 stainless steel and Cr₃C₂ powder. *J Mater Process Technol* 209:5229–5238. <https://doi.org/10.1016/j.jmatprotec.2009.03.010>
19. Zhang DW, Lei TC (2003) The microstructure and erosive-corrosive wear performance of laser-clad Ni-Cr₃C₂ composite coating. *Wear* 255:129–133. [https://doi.org/10.1016/S0043-1648\(03\)00283-7](https://doi.org/10.1016/S0043-1648(03)00283-7)
20. Sun GF, Zhang YK, Liu CS, Luo KY, Tao XQ, Li P (2010) Microstructure and wear resistance enhancement of cast steel rolls by laser surface alloying NiCr-Cr₃C₂. *Mater Des* 31:2737–2744. <https://doi.org/10.1016/j.matdes.2010.01.021>
21. Bendikiene R, Ciuplys A, Mindaugas Jankus S, Surzhenkov A, Tkachivskiy D, Juhani K, Viljus M, Traksmas R, Antonov M, Kulu P (2019) Study of submerged and plasma arc welded composite hardfacings with a novel Cr₃C₂-Ni reinforcement. *P Est Acad Sci* 68:1–8
22. Theiler C, Seefeld T, Schubert E, Sepold G (1998) Laser beam cladding of graded layers and freeform components. Proceedings of the ECLAT, Werkstoff-Informationgesellschaft, Frankfurt, Germany
23. Venkatesh L, Samajdar I, Tak M, Doherty RD, Gundakaram RC, Prasad KS, Joshi SV (2015) Microstructure and phase evolution in laser clad chromium carbide-NiCrMoNb. *Appl Surf Sci* 357:2391–2401. <https://doi.org/10.1016/j.apsusc.2015.09.260>
24. Grainger S, Blunt J (1998) Engineering coatings – design and application, second edn. Abington Publishing, Cambridge
25. Directorate-General for Internal Market, Industry, Entrepreneurship and SMEs (European Commission) (2020) Study on the EU's list of critical raw materials - Critical raw materials factsheets
26. Special Metals Corporation (2013) INCONEL® alloy 625. www.specialmetals.com
27. Tuominen J (2009) Engineering coatings by laser cladding – the study of wear and corrosion properties. Tampere University of Technology, Dissertation
28. Martukanitz RP, Tressler JF, JH MD (2007) Deposition efficiencies of laser cladding with various sources. In: Proceedings of the ICALEO, 2007. Laser Institute of America, Orlando, USA
29. Venkatesh LR, Babu PS, Gundakaram RC, Doherty RD, Joshi SV, Samajdar I (2017) Morphology-dependent hardness of Cr₇C₃-Ni-rich alloy composite vs orientation independent hardness of Cr₇C₃ primary phase in a laser clad microstructure. *Metall Mater Trans A* 48A:1534–1539. <https://doi.org/10.1007/s11661-017-3984-2>
30. Anthonysamy S, Ananthasivan K, Kaliappan I, Chandramouli V, Vasudeva Rao PR, Mathews CK, Jacob KT (1996) Gibbs energies of formation of chromium carbides. *Metall Mater Trans A* 27A:1919–1924
31. Näkki J (2018) Properties of Alloy 625 claddings made with laser and CMT methods. Tampere University of Technology, Dissertation
32. Kurz W, Fisher DJ (1989) Fundamentals of solidification, 3rd edn. Trans Tech Publications, Switzerland
33. Tinoco J, Fredriksson H (2004) Solidification of a modified Inconel 625 alloy under different cooling rates. *High Temp Mat Pr* 23:13–24
34. Goodhew PJ, Humphreys J (2017) Electron microscopy and analysis, 3rd edn. CRC Press, Boca Raton
35. Haukaas-Eide O, Lønvik K (2010) Guideline for qualification of wear and corrosion protection surface materials for piston rods (revised 2010). DNV Technical Report No. 2009–3295, p 59
36. Kagawa A, Ohta Y (1995) Wear resistance of laser clad chromium carbide surface layers. *Mater Sci Technol* 11:515–519. <https://doi.org/10.1179/mst.1995.11.5.515>
37. Department of Trade and Industry (1986) Wear resistant surfaces in engineering: a guide to their production, properties and selection, first edn. Crown, UK
38. Jones AR (1989) Microcracks in hard chromium electrodeposits. *Plat Surf Finish* 76(4):62–66
39. Tuominen J, Näkki J, Pajukoski H, Miettinen J, Peltola T, Vuoristo P (2015) Wear and corrosion resistant laser coatings for hydraulic piston rods. *J Laser Appl* 27:022009-1–022009-12. <https://doi.org/10.2351/1.4914503>
40. Wang J, Zhang Q, Shen W, Liang Z, Chang C, Yang L, Li J, Huang F (2022) Failure analysis of a chromium plating layer on a piston rod surface and the study of Ni-based composite coating with Nb addition by laser cladding. *Metals* 12:1194. <https://doi.org/10.3390/met12071194>
41. McMahon MA, Green A, Watkins KG, Ferreira MGS, Vilar R (1995) Effect of residual stress on the corrosion properties of CO₂ laser surface melted alloys. *Mater Sci Forum* 192-194:789–796
42. Chon XY, Jiang YJ, Zhou R, Feng J (2017) Multialloying effect on thermophysical properties of Cr₇C₃-type carbides. *J Am Ceram Soc* 100:1588–1597
43. Kadolkar PB, Watkins TR, Dahotre N (2002) Residual stress characterization of particulate-reinforced composite coating using X-ray diffraction technique. In: Proceedings from the 1st International Surface Engineering Congress and the 13th IFHTSE Congress. Columbus, USA, pp 593–603
44. Tuominen J, Vuoristo P (2007) Induction heating unit equipped with closed-loop PID controller; versatile tool in laser cladding. In: Proceedings of the International Congress on Applications of Lasers & Electro-Optics. Laser Institute of America, Orlando, FL, USA

Publisher's note Springer Nature remains neutral with regard to jurisdictional claims in published maps and institutional affiliations.